Analysis and Experimental Verification for Dynamic Modeling of A Skid-Steered Wheeled Vehicle

Wei Yu, *Student Member, IEEE*, Oscar Ylaya Chuy, Jr., *Member, IEEE*, Emmanuel G. Collins, Jr., *Senior Member, IEEE*, and Patrick Hollis

Abstract—**Skid-steered vehicles are often used as outdoor mobile robots due to their robust mechanical structure and high maneuverability. Sliding, along with rolling, is inherent to general curvilinear motion, which makes both kinematic and dynamic modeling difficult. For the purpose of motion planning, this paper develops and experimentally verifies dynamic models of a skid-steered wheeled vehicle for general planar (2-D) motion and for linear 3-D motion. These models are characterized by the coefficient of rolling resistance, the coefficient of friction, and the shear deformation modulus, which have terrain-dependent values. The dynamic models also include motor saturation and motor power limitations, which enable correct prediction of vehicle velocities when traversing on hills. It is shown that the closed-loop system that results from inclusion of the dynamics of the [proportional–integral–derivative (PID)] speed controllers for each set of wheels does a much better job than the open-loop model of predicting the vehicle linear and angular velocities. For a vehicle turning with small linear and angular accelerations, the model provides accurate predictions of velocities and reasonable predictions of torques. Hence, the closed-loop model is recommended for motion planning.**

Index Terms—**Closed-loop control, dynamic modeling, path planning, proportional–integral–derivative (PID), skid-steered wheeled robot, velocity and torque prediction.**

I. INTRODUCTION

DYNAMIC models of autonomous ground vehicles are needed to enable realistic motion planning [1] in unstructured, outdoor environments that have substantial changes in elevation, consist of a variety of terrain surfaces, and/or require frequent accelerations and decelerations. At least four different motion planning tasks can be accomplished using appropriate dynamic models.

1) *Time optimal motion planning:* A dynamic model can yield good predictions of a vehicle's velocity as it traverses a hill or gulley of a particular terrain, including the maximum climbing velocity of a given hill, the estimation of the needed entry velocities to climb steep hills, and the prediction of whether a vehicle is even capable of climbing a hill. These predictions are key to computing the time-optimal trajectories, and hence, the dynamic model is important for motion planning in an undulating environment.

2) *Energy efficient motion planning:* This type of planning is important, since finite energy availability is a critical constraint that must be taken into account when planning motion for vehicles. A dynamic model provides predictions of torque and velocity and, hence, the power and energy consumption. Related capabilities are the ability to predict whether a given task can be completed with the vehicle's current energy supply and estimations of when to refuel or recharge.

3) *Reduction in the frequency of replanning:* One of the primary reasons that replanning is necessary is due to discrepancies between the predicted and actual vehicle motion. Since a dynamic model can lead to more accurate motion predictions in planning, it can reduce the frequency of replanning.

4) *Planning in the presence of a fault, such as flat tire or faulty motor:* A dynamic model includes the motor properties, and the tire and ground interaction. Common vehicle faults are faulty motors or flat tires. Their influence on vehicle motion can be captured by the dynamic model utilized to plan the vehicle trajectories. The dynamic model will enable more efficient mobility in the presence of these faults.

For the purpose of motion planning, this paper develops dynamic models of a skid-steered wheeled vehicle to help the aforementioned motion planning tasks.

Ackerman steering, differential steering, and skid steering are the most widely used steering mechanisms for wheeled and tracked vehicles. Ackerman steering has the advantages of good lateral stability when turning at high speeds, good controllability [2], and lower power consumption [3] but has the disadvantages of low maneuverability and the need for an explicit mechanical steering subsystem [2]–[4]. Differential steering is popular because it provides high maneuverability with a zero turning radius and has a simple steering configuration [2], [5]. However, it does not have strong traction and mobility over rough and loose terrain and, hence, is seldom used for outdoor terrains. Like differential steering, skid steering leads to high maneuverability [2], [6], [7] and faster response [8] and has a simple [3], [4], [9] and robust mechanical structure [4], [10], [11]. In contrast, it also leads to strong traction and high mobility [9], which makes it suitable for all-terrain traversal.

A skid-steered vehicle can be characterized by two features [2], [4]. First, the vehicle steering depends on controlling the relative velocities of the left and right side wheels or tracks. Second, all wheels or tracks remain parallel to the longitudinal axis of the vehicle, and vehicle turning requires slippage of the wheels or tracks. Due to identical steering mechanisms, wheeled and tracked skid-steered vehicles share many properties [4], [10], [12], [13]. Many of the difficulties associated with modeling and operating both classes of skid-steered vehicles arise from the complex wheel (or track) and terrain interaction [4], [13]. For Ackerman-steered or differential-steered vehicles, the wheel motions may often be accurately modeled by pure rolling, while for skid-steered vehicles, in general, are modeled by curvilinear motion, the wheels (or tracks) roll and slide at the same time [4], [10], [13], [14]. This makes it difficult to develop kinematic and dynamic models, which accurately describe the motion. Other disadvantages are that the motion tends to be energy inefficient and difficult to control [8], [11], and for wheeled vehicles, the tires tend to wear out faster [15].

A kinematic model of a skid-steered wheeled vehicle maps the wheel velocities to the vehicle velocities and is an important component in the development of a dynamic model. In contrast to the kinematic models for Ackerman-steered and differential-steered vehicles, the kinematic model of a skid-steered vehicle is dependent on more than the physical dimensions of the vehicle, since it must take into account vehicle sliding and is hence terrain-dependent [4], [16]. In [4] and [8], a kinematic model of a skid-steered vehicle was developed by assuming a certain equivalence with a kinematic model of a differential-steered vehicle. This was accomplished by experimentally determining the instantaneous centers of rotation (ICRs) of the sliding velocities of the left and right wheels. An alternative kinematic model that is based on the slip ratios of the wheels has been presented in [12] and [16]. This model takes into account the longitudinal slip ratios of the left and right wheels. The difficulty in using this model is the actual detection of slip, which cannot be computed analytically. Hence, developing practical methods to experimentally determine the slip ratios is an active research area [17]–[20].

To date, there is very little published research on the experimentally verified dynamic models for general motion of skid-steered vehicles, especially wheeled vehicles. The main reason is that it is hard to model the tire (or track) and terrain interaction when slipping and skidding occur. (For each vehicle wheel, if the wheel linear velocity computed using the angular velocity of the wheel is larger than the actual linear velocity of the wheel, slipping occurs, while if the computed wheel velocity is smaller than the actual linear velocity, skidding occurs.) The research of [6] developed a dynamic model for planar motion by considering longitudinal rolling resistance, lateral friction, moment of resistance for the vehicle, and the nonholonomic constraint for lateral skidding. In addition, a model-based nonlinear controller was designed for trajectory tracking. However, this model uses Coulomb friction to describe the lateral sliding friction and moment of resistance, which contradicts the experimental results [16], [21]. In addition, it considers none of the

motor properties. Furthermore, the results of [6] are limited to simulation without experimental verification.

The research in [11] developed a planar dynamic model of a skid-steered vehicle, which is essentially that of [6], using a different velocity vector (consisting of the longitudinal and angular velocities of the vehicle instead of the longitudinal and lateral velocities). In addition, the dynamics of the motors, although not the power limitations, were added to the model. Kinematic, dynamic, and motor-level control laws were explored for trajectory tracking. However, as in [6], Coulomb friction was used to describe the lateral friction and moment of resistance, and the results are limited to simulation.

In [13], a functional relationship between the coefficient of friction and longitudinal slip is used to capture the interaction between the wheels and ground and, further, to develop a dynamic model of skid-steered wheeled vehicle. Also, an adaptive controller is designed to enable the robot to follow a desired trajectory. The inputs of the dynamic model are the longitudinal slip ratios of the four wheels. However, the longitudinal slip ratios are difficult to measure in practice and depend on the terrain surface, instantaneous radius of curvature, and vehicle velocity. In addition, no experiment is conducted to verify the reliability of the torque prediction from the dynamic model and motor saturation, and power limitations are not considered. In [22], the dynamic model from [13] is used to explore the motion stability of the vehicle, which is controlled to move with constant linear velocity and angular velocity for each half of a lemniscate to estimate wheel slip. As in [13], no experiment is carried out to verify the fidelity of the dynamic model.

The most thorough dynamic analysis of a skid-steered vehicle is found in [16] and [21], which consider steady-state (i.e., constant linear and angular velocities) dynamic models for circular motion of *tracked* vehicles. A primary contribution of this research is that it proposes and then provides experimental evidence that in the track–terrain interaction, the shear stress is a particular function of the shear displacement (see (7) of Section III). This model differs from the Coulomb model of friction, adopted in [6] and [11], which essentially assumes that the maximum shear stress is obtained as soon as there is any relative movement between the track and the ground. This research also provides detailed analysis of the longitudinal and lateral forces that act on a tracked vehicle, but their results had not been extended to skid-steered *wheeled* vehicles. In addition, they do not consider vehicle acceleration, terrain elevation, actuator limitations, or the vehicle control system.

Based upon the research in [16] and [21], this paper develops dynamic models of a skid-steered wheeled vehicle for general curvilinear planar (2-D) motion and straight-line 3-D motion. As in [16] and [21], the modeling is based upon the functional relationship of shear stress to shear displacement. Practically, this means that for a vehicle tire, the shear stress varies with the turning radius. This research also includes models of the saturation and power limitations of the actuators as part of the overall vehicle model. In addition, it shows that the closed-loop model yields substantially better predictions of the vehicle velocity than the corresponding open-loop model.
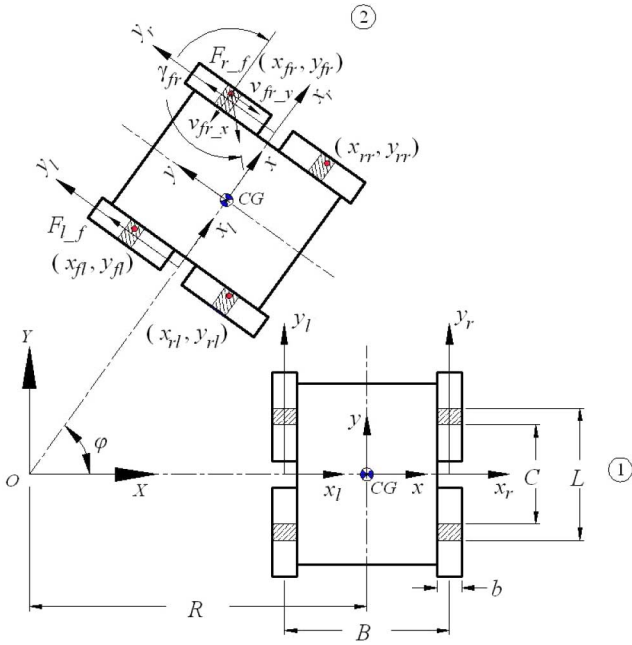
Fig. 1.   Circular motion of a skid-steered wheeled vehicle.

Preliminary research results on modeling of skid-steered vehicles can be found in [14] and [23]. This paper is an extension of this previous work. Here, we not only describe the open-loop dynamic model, but we also detail the models of the additional components of the closed-loop system: the proportional–integral–derivative (PID) controller, motor saturation, and motor power limitations. Also, the experiments now include the very important case of general curvilinear motion, which consists of continuously changing linear and angular velocities.

The remainder of this paper is organized as follows. Section II describes the terrain-dependent kinematic model needed for the development of the dynamic model. Section III discusses the wheel and terrain interaction of a skid-steered wheeled vehicle and establishes the dynamic models. Section IV describes the closed-loop model, including the discussion of the PID controller, motor, and motor controller. Section V experimentally verifies the dynamic models in planar and hill-climbing experiments. Finally, Section VI concludes the paper and discusses future research.

II. KINEMATIC MODELS

In this section, the kinematic model of a skid-steered wheeled vehicle is described and discussed. It is an important component in the development of the overall dynamic model of a skid-steered vehicle.

To mathematically describe the kinematic models that have been developed for skid-steered vehicles, consider a wheeled vehicle moving at constant velocity about an ICR (see Fig. 1). The local coordinate frame, which is attached to the body center of gravity (CG), is denoted by x–y, where x is the lateral coordinate, and y is the longitudinal coordinate.

When a skid-steered vehicle rotates, the inner wheel experiences longitudinal skidding, while the outer wheel experiences longitudinal slipping. The lateral sliding velocity is relatively

small [4], [8], [18] and, hence, is neglected in this paper. For vehicles that are symmetric about the x and y axes, an ideal symmetric experimental kinematic model of a skid-steered wheeled vehicle is given by [4]

$$\begin{bmatrix} v_y \\ \dot{\varphi} \end{bmatrix} = \frac{r}{\alpha B} \begin{bmatrix} \dfrac{\alpha B}{2} & \dfrac{\alpha B}{2} \\ -1 & 1 \end{bmatrix} \begin{bmatrix} \omega_l \\ \omega_r \end{bmatrix} \tag{1}$$

where ω_l and ω_r are the angular velocities of the left and right wheels, respectively, v_y is the vehicle velocity in the longitudinal direction, $\dot{\varphi}$ is the vehicle angular velocity, B is the vehicle width, r is the wheel radius, and α is a terrain-dependent parameter that is a function of the ICRs. (Note that the lateral velocity $v_x = 0$.) Our experimental results show that the larger the rolling resistance, the larger the value of α. For a Pioneer 3-AT mobile robot (see Fig. 7), $\alpha = 1.5$ for a vinyl laboratory surface and $\alpha > 2$ for a concrete surface. (More experiments are needed to obtain the precise α for a concrete surface.) Equation (1) shows that the kinematic model of a skid-steered wheeled vehicle of width B is equivalent to the kinematic model of a differential-steered wheeled vehicle of width αB.

A more rigorously derived kinematic model for a skid-steered vehicle is presented in [12] and [16]. This model takes into account the longitudinal slip ratios i_l and i_r of the left and right wheels and, for symmetric vehicles, is given by

$$\begin{bmatrix} v_y \\ \dot{\varphi} \end{bmatrix} = \frac{r}{B} \begin{bmatrix} \dfrac{(1-i_l)B}{2} & \dfrac{(1-i_r)B}{2} \\ -(1-i_l) & (1-i_r) \end{bmatrix} \begin{bmatrix} \omega_l \\ \omega_r \end{bmatrix} \tag{2}$$

where $i_l \triangleq (r\omega_l - v_{l\_a})/(r\omega_l)$, $i_r \triangleq (r\omega_r - v_{r\_a})/(r\omega_r)$, and v_{l_a} and v_{r_a} are the actual velocities of the left and right wheels. We have found that when

$$\frac{i_l}{i_r} = -\frac{\omega_r}{\omega_l} \quad \text{and} \quad \alpha = \frac{1}{1 - (2i_l i_r)/(i_l + i_r)} \tag{3}$$

(1) and (2) are identical. Currently, to our knowledge, no analysis or experiments have been performed to verify the left-hand equation in (3) and analyze its physical significance.

III. DYNAMIC MODELS

This section develops dynamic models of a skid-steered wheeled vehicle for the cases of general 2-D motion and linear 3-D motion. In contrast to dynamic models described in terms of the velocity vector of the vehicle [6], [11], the dynamic models here are described in terms of the angular velocity vector of the wheels. This is because the wheel (specifically, the motor) velocities are actually commanded by the control system; therefore, this model form is particularly beneficial for control and planning.

Following [11], the dynamic model considering the nonholonomic constraint is given by

$$M\ddot{q} + C(q, \dot{q}) + G(q) = \tau \tag{4}$$

where $q = [\theta_l \ \theta_r]^T$ is the angular displacement of the left and right wheels, $\dot{q} = [\omega_l \ \omega_r]^T$ is the angular velocity of the left and right wheels, $\tau = [\tau_l \ \tau_r]^T$ is the torque of the left and right

motors, M is the mass matrix, $C(q, \dot{q})$ is the resistance term, and $G(q)$ is the gravitational term. The primary focus of the following section is the derivation of $C(q, \dot{q})$ to properly model the ground and wheel interaction.

A. 2-D General Motion

When the vehicle is moving on a 2-D surface, it follows from the model given in [11], which is expressed in the local x–y coordinates and the kinematic model (1) that M in (4) is given by

$$M = \begin{bmatrix} \dfrac{mr^2}{4} + \dfrac{r^2 I}{\alpha B^2} & \dfrac{mr^2}{4} - \dfrac{r^2 I}{\alpha B^2} \\ \dfrac{mr^2}{4} - \dfrac{r^2 I}{\alpha B^2} & \dfrac{mr^2}{4} + \dfrac{r^2 I}{\alpha B^2} \end{bmatrix} \quad (5)$$

where m and I are the mass and moment of inertia of the vehicle, respectively. Since we are considering planar motion $G(q) = 0$. $C(q, \dot{q})$ represents the resistance resulting from the interaction of the wheels and terrain, including the rolling resistance, sliding frictions, and the moment of resistance, the latter two of which are modeled using Coulomb friction in [6] and [11]. Assume that $\dot{q} = [\omega_l \ \omega_r]^T$ is a known constant; then, $\ddot{q} = 0$, and (4) becomes

$$C(q, \dot{q}) = \tau. \quad (6)$$

The remainder of this section describes how we apply this constant velocity analysis to the development of an analytical expression for $C(q, \dot{q})$. The inputs to (8)–(16), shown below, are the left and right wheel angular velocities ω_l and ω_r. We begin by describing the relationship between the shear stress and shear displacement associated with the sliding of the wheel over the terrain [see (7), shown below]. Then, the constant angular velocities for the left and right wheels (ω_l and ω_r) are used to determine the wheel sliding velocities [see (9) and (11), shown below]. Then, we use the sliding velocities to derive the shear displacements of the wheels [see (12)–(16), shown below]. Using (7), the corresponding shear stresses are integrated over the contact patch to obtain the frictional forces [see (17) and (20), shown below], which along with the rolling resistances determine the resistance term $C(q, \dot{q})$ [see (18), (19), (21), and (22), shown below].

Previous research [6], [11] assumed that the shear stress takes on its maximum magnitude as soon as a small relative movement occurs between the contact surface of the wheel and terrain. Instead of using this theory for tracked vehicle, [16] and [21] present experimental evidence to show that the shear stress of the tread is function of the shear displacement. The maximum shear stress is practically achieved only when the shear displacement exceeds a particular threshold. In this section, this theory will be applied to a skid-steered wheeled vehicle.

Based on the theory in [16] and [21], the shear stress τ_{ss} and shear displacement j relationship can be described as follows:

$$\tau_{\text{ss}} = p\mu(1 - e^{-j/K}) \quad (7)$$

where p is the normal pressure, μ is the coefficient of friction, and K is the shear deformation modulus. K is a terrain-dependent parameter, like the rolling resistance and coefficient of friction [16].

Fig. 1 depicts a skid-steered wheeled vehicle moving counterclockwise (CCW) at constant linear velocity v and angular velocity $\dot{\varphi}$ in a circle centered at O from position 1 to position 2. X–Y denotes that the global frame and the body-fixed frames for the right and left wheels are given by the x_r–y_r and x_l–y_l, respectively. The four contact patches of the wheels with the ground are shadowed in Fig. 1, and L and C are the patch-related distances shown in Fig. 1. It is assumed that the vehicle is symmetric and that the CG is at the geometric center. Note that because ω_l and ω_r are known, v_y and $\dot{\varphi}$ can be computed using the vehicle kinematic model (1), which enables the determination of the radius of curvature R, since $v_y = R\dot{\varphi}$.

In the x_r–y_r frame, consider an arbitrary point on the contact patch of the front right wheel with coordinates $(x_{\text{fr}}, y_{\text{fr}})$. This contact patch is *not* fixed on the tire but is the part of the tire that contacts the ground. The time interval t for this point to travel from an initial contact point $(x_{\text{fr}}, L/2)$ to $(x_{\text{fr}}, y_{\text{fr}})$ is as follows:

$$t = \int_{y_{\text{fr}}}^{L/2} \frac{1}{r\omega_r} dy_r = \frac{L/2 - y_{\text{fr}}}{r\omega_r}. \quad (8)$$

At the same time, the vehicle has moved from position 1 to position 2 with an angular displacement of φ. The sliding velocities of point $(x_{\text{fr}}, y_{\text{fr}})$ in the x_r and y_r directions are denoted by v_{fr_x} and v_{fr_y}. Therefore

$$v_{\text{fr}\_x} = -y_{\text{fr}}\dot{\varphi}, \quad v_{\text{fr}\_y} = \left(R + \frac{B}{2} + x_{\text{fr}}\right)\dot{\varphi} - r\omega_r. \quad (9)$$

The resultant sliding velocity v_{fr} and its angle γ_{fr} in the x_r–y_r frame are as follows:

$$v_{\text{fr}} = \sqrt{v_{\text{fr}\_x}^2 + v_{\text{fr}\_y}^2}, \quad \gamma_{\text{fr}} = \pi + \arctan\left(\frac{v_{\text{fr}\_y}}{v_{\text{fr}\_x}}\right). \quad (10)$$

Note that when the wheel is sliding, the direction of friction is opposite from the sliding velocity, and if the vehicle is in pure rolling, v_{fr_x} and v_{fr_y} are zero.

In order to calculate the shear displacement of this reference point, the sliding velocities need to be expressed in the global X–Y frame. Let v_{fr_X} and v_{fr_Y} denote the sliding velocities in the X- and Y-directions. Then, the transformation between the local and global sliding velocities is given by

$$\begin{bmatrix} v_{\text{fr}\_X} \\ v_{\text{fr}\_Y} \end{bmatrix} = \begin{bmatrix} \cos\varphi & -\sin\varphi \\ \sin\varphi & \cos\varphi \end{bmatrix} \begin{bmatrix} v_{\text{fr}\_x} \\ v_{\text{fr}\_y} \end{bmatrix}. \quad (11)$$

The shear displacements j_{fr_X} and j_{fr_Y} in the X- and Y-directions can be expressed as follows:

$$\begin{aligned} j_{\text{fr}\_X} &= \int_0^t v_{\text{fr}\_X} dt = \int_{y_{\text{fr}}}^{L/2} (v_{\text{fr}\_x}\cos\varphi - v_{\text{fr}\_y}\sin\varphi)\frac{1}{r\omega_r}dy_r \\ &= \left(R + \frac{B}{2} + x_{\text{fr}}\right)\left\{\cos\left[\frac{(L/2 - y_{\text{fr}})\dot{\varphi}}{r\omega_r}\right] - 1\right\} \\ &\quad - y_{\text{fr}}\sin\left[\frac{(L/2 - y_{\text{fr}})\dot{\varphi}}{r\omega_r}\right] \end{aligned} \quad (12)$$

$$j_{\text{fr}\_Y} = \int_0^t v_{\text{fr}\_Y}\,dt = \int_{y_{\text{fr}}}^{L/2} (v_{\text{fr}\_x}\sin\varphi + v_{\text{fr}\_y}\cos\varphi)\frac{1}{r\omega_r}\,dy_r$$

$$= \left(R + \frac{B}{2} + x_{\text{fr}}\right)\sin\left[\frac{(L/2 - y_{\text{fr}})\dot\varphi}{r\omega_r}\right] - \frac{L}{2}$$

$$+ y_{\text{fr}}\cos\left[\frac{(L/2 - y_{\text{fr}})\dot\varphi}{r\omega_r}\right]. \tag{13}$$

The resultant shear displacement j_{fr} in the X–Y frame is given by $j_{\text{fr}} = \sqrt{j_{\text{fr}\_X}^2 + j_{\text{fr}\_Y}^2}$. Similarly, it can be shown that for the reference point $(x_{\text{rr}}, y_{\text{rr}})$ in the rear right wheel the angle of the sliding velocity γ_{rr} in the x_r–y_r frame is as follows:

$$\gamma_{\text{rr}} = \arctan\left[\frac{(R + B/2 + x_{\text{rr}})\dot\varphi - r\omega_r}{-y_{\text{rr}}\dot\varphi}\right] \tag{14}$$

the shear displacements j_{rr_X} and j_{rr_Y} are given by

$$j_{\text{rr}\_X} = \left(R + \frac{B}{2} + x_{\text{rr}}\right)\left\{\cos\left[\frac{(-C/2 - y_{\text{rr}})\dot\varphi}{r\omega_r}\right] - 1\right\}$$

$$- y_{\text{rr}}\sin\left[\frac{(-C/2 - y_{\text{rr}})\dot\varphi}{r\omega_r}\right] \tag{15}$$

$$j_{\text{rr}\_Y} = \left(R + \frac{B}{2} + x_{\text{rr}}\right)\sin\left[\frac{(-C/2 - y_{\text{rr}})\dot\varphi}{r\omega_r}\right] + \frac{C}{2}$$

$$+ y_{\text{rr}}\cos\left[\frac{(-C/2 - y_{\text{rr}})\dot\varphi}{r\omega_r}\right] \tag{16}$$

and the magnitude of the resultant shear displacement j_{rr} is $j_{\text{rr}} = \sqrt{j_{\text{rr}\_X}^2 + j_{\text{rr}\_Y}^2}$.

The friction force points in the opposite direction of the sliding velocity. Using j_{fr} and j_{rr}, derived earlier with (7) and integrating along the contact patches yields that the longitudinal sliding friction of the right wheels F_{r_f} can be expressed as follows:

$$F_{r\_f} = \int_{C/2}^{L/2}\int_{-b/2}^{b/2} p_r\mu_r(1 - e^{-j_{\text{fr}}/K_r})\sin(\pi + \gamma_{\text{fr}})dx_r\,dy_r$$

$$+ \int_{-L/2}^{-C/2}\int_{-b/2}^{b/2} p_r\mu_r(1 - e^{-j_{\text{rr}}/K_r})\sin(\pi + \gamma_{\text{rr}})dx_r\,dy_r \tag{17}$$

where p_r, μ_r, and K_r are the normal pressure, coefficient of friction, and shear deformation modulus of the right wheels, respectively. While most of the parameters in (17) can be directly measured, as discussed next, the parameters μ_r and K_r must be estimated.

Let f_{r_r} denote the rolling resistance of the right wheels, including the internal locomotion resistance, such as resistance from belts, motor windings, and gearboxes [24]. The complete resistance torque τ_{r_Res} from the ground to the right wheel is given by

$$\tau_{r\_\text{Res}} = r(F_{r\_f} + f_{r\_r}). \tag{18}$$

Since ω_r is constant, the input torque τ_r from right motor will compensate for the resistance torque, such that

$$\tau_r = \tau_{r\_\text{Res}}. \tag{19}$$

It follows that experiments that measure τ_r can be used to estimate the parameters μ_r and K_r. A procedure for performing this estimation is given in Section V.

The earlier discussion is for the right wheels. Exploiting the same derivation process, one can obtain analytical expressions for the shear displacements j_{fl} and j_{rl} of the front and rear left wheels and the angles of the sliding velocity γ_{fl} and γ_{rl}. The longitudinal sliding friction of the left wheels F_{l_f} is then given by

$$F_{l\_f} = \int_{C/2}^{L/2}\int_{-b/2}^{b/2} p_l\mu_l(1 - e^{-j_{\text{fl}}/K_l})\sin(\pi + \gamma_{\text{fl}})dx_l\,dy_l$$

$$+ \int_{-L/2}^{-C/2}\int_{-b/2}^{b/2} p_l\mu_l(1 - e^{-j_{\text{rl}}/K_l})\sin(\pi + \gamma_{\text{rl}})dx_l\,dy_l \tag{20}$$

where p_l, μ_l, and K_l are the normal pressure, coefficient of friction, and shear deformation modulus of the left wheels, respectively. Let f_{l_r} denote the rolling resistance of the left wheels. The input torque τ_l of the left motor equals the resistance torque of the left wheel τ_{l_Res}, such that

$$\tau_l = \tau_{l\_\text{Res}} = r(F_{l\_f} + f_{l\_r}). \tag{21}$$

Using (19) and the left equation of (21) with (6) yields

$$C(q, \dot q) = [\tau_{l\_\text{Res}}\,\tau_{r\_\text{Res}}]^T. \tag{22}$$

Substituting (5), (22), and $G(q) = 0$ into (4) yields a dynamic model that can be used to predict 2-D movement for the skid-steered vehicle

$$\begin{bmatrix} \dfrac{mr^2}{4} + \dfrac{r^2 I}{\alpha B^2} & \dfrac{mr^2}{4} - \dfrac{r^2 I}{\alpha B^2} \\[2ex] \dfrac{mr^2}{4} - \dfrac{r^2 I}{\alpha B^2} & \dfrac{mr^2}{4} + \dfrac{r^2 I}{\alpha B^2} \end{bmatrix}\ddot q + \begin{bmatrix} \tau_{l\_\text{Res}} \\[1ex] \tau_{r\_\text{Res}} \end{bmatrix} = \begin{bmatrix} \tau_l \\[1ex] \tau_r \end{bmatrix}. \tag{23}$$

In summary, in order to obtain (22), the shear displacement calculation of (12), (13), (15), and (16) is the first step. The inputs to these equations are the left and right wheel angular velocities ω_l and ω_r. The shear displacements are employed in (17) and (20) to obtain the right and left sliding friction forces F_{r_f} and F_{l_f}. Next, the sliding friction forces and rolling resistances are substituted into (18) and (21) to calculate the right and left resistance torques, which determine $C(q, \dot q)$ using (22).

B. 3-D Linear Motion

For 3-D linear motion, each wheel of the skid-steered vehicle can be assumed to be in pure rolling. The F_{r_f} in (18) and F_{l_f} in (21) are zero. Fig. 2 is the free body diagram of a skid-steered wheeled vehicle for this case. It is assumed that the surface elevation is described by $Z = f(Y)$, such that the left and right front wheels experience the same elevation and likewise for the rear wheels. Let β denote the angle between the global coordinate axis Y and the body-fixed axis y_r [which can be determined analytically from $Z = f(Y)$], W is the weight of vehicle, f_{r_r} is the rolling resistance of the right wheels, and F_r is the traction force that acts on the vehicle. The left wheel forces
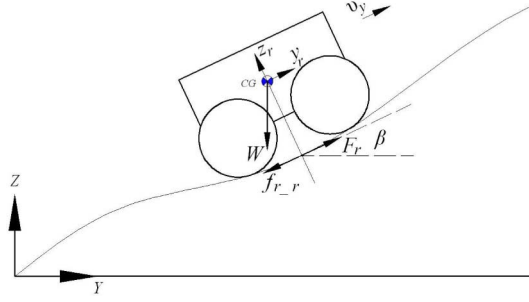
Fig. 2. Free-body diagram for vehicle hill climbing.

are identical to those of the right wheels and are not shown in Fig. 2.

The gravitational term $G(q)$ is generally nonzero and is given by

$$G(q) = \frac{mgr\sin\beta}{2}\begin{bmatrix} 1 & 1 \end{bmatrix}^T. \tag{24}$$

Substituting (5), (22), and (24) into (4) yields a dynamic model that can be used to predict 3-D motion, given the assumption $Z = f(Y)$:

$$\begin{bmatrix} \dfrac{mr^2}{4} + \dfrac{r^2 I}{\alpha B^2} & \dfrac{mr^2}{4} - \dfrac{r^2 I}{\alpha B^2} \\ \dfrac{mr^2}{4} - \dfrac{r^2 I}{\alpha B^2} & \dfrac{mr^2}{4} + \dfrac{r^2 I}{\alpha B^2} \end{bmatrix} \ddot{q} + \begin{bmatrix} \tau_{l\_\text{Res}} \\ \tau_{r\_\text{Res}} \end{bmatrix}$$
$$+ \begin{bmatrix} \dfrac{mgr\sin\beta}{2} \\ \dfrac{mgr\sin\beta}{2} \end{bmatrix} = \begin{bmatrix} \tau_l \\ \tau_r \end{bmatrix}. \tag{25}$$

For the experimental verification in Section V, β is constant, since the experiments were performed on surfaces with constant slopes.

IV. CLOSED-LOOP CONTROL SYSTEM

The dynamic models described earlier are essential parts of simulation models used to predict the vehicle motion. However, no matter how detailed the analysis, these models will have uncertain parameters, e.g., the coefficient of rolling resistance, coefficient of friction, and shear modulus.

The models of open-loop and closed-loop control systems that can be utilized to predict motion are shown in Fig. 3 for one side of the vehicle. The complete control system for the vehicle is the combination of the two control systems for each side of the vehicle. The open-loop system consists of four parts: vehicle dynamics, terrain interaction, motor, and motor controller. The closed-loop control system additionally includes the PID speed controller for the motor in a unity feedback. As is experimentally illustrated in Fig. 16, the open-loop system is highly sensitive to these uncertainties and, hence, can yield poor velocity predictions, while the feedback system can dramatically reduce the effects of the model uncertainty. In most of the experimental results described in the next section, the closed-loop model is employed as the simulation model.
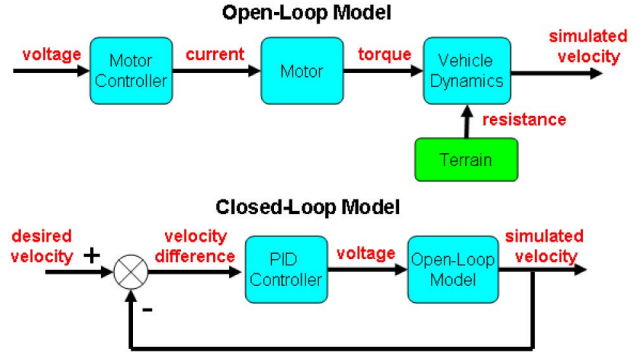

Fig. 3. Open-loop and closed-loop control systems for the left or right side of a skid-steered wheeled vehicle.
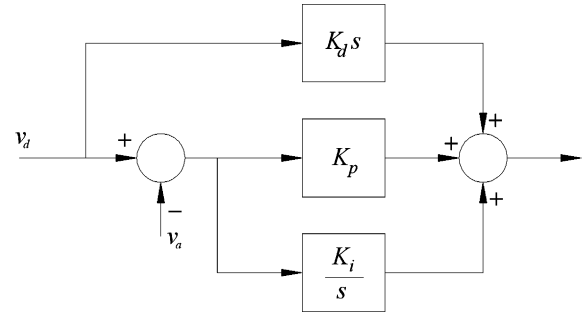

Fig. 4. Modified PID controller.

The vehicle dynamics and terrain–vehicle interaction were described in Section III. The remaining three parts, i.e., the PID controller, motor, and motor controller, are described next.

A. PID Controller

In our research, a modified PID controller in Fig. 4, for which the input to the derivative term is the reference signal, not the error signal, was adopted from [25]. The variables v_d and v_a are the desired velocity and actual velocity. The PID parameters are tuned by following the rules from [25, ch. 9].

B. Motor

The moment of inertia and viscous friction of the motor are given in Table II and are small with respect to the vehicle inertia and friction (also shown in Table II). Hence, the dynamics of the motor have been neglected. However, the speed versus current curve for a dc motor was used to model the motor.

In the following, τ_m, I_m, and ω_m are the torque, current, and angular velocity of the motor, respectively, τ_s is the stall torque, ω_n is the no-load speed, $\tau_{\max}$ is the maximum continuous torque, $I_{\max}$ is the maximum continuous current, and V_m is the motor voltage. Fig. 5 shows the torque–speed property of the dc motor, which can be expressed as follows [26]:

$$\frac{\tau_m}{\tau_s} + \frac{\omega_m}{\omega_s} = 1 \tag{26}$$

where

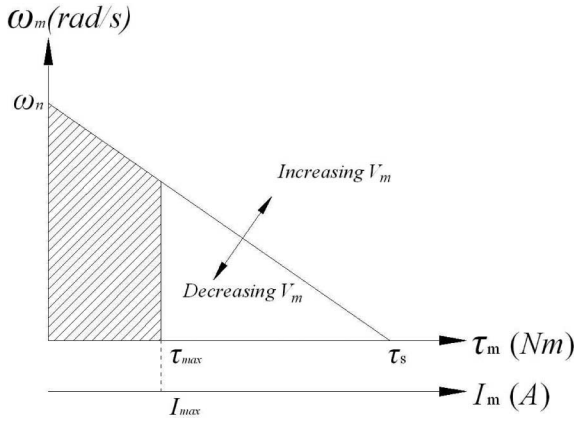$$\tau_s = \frac{V_m K_T}{R_a}, \qquad \omega_s = \frac{V_m}{K_B}$$

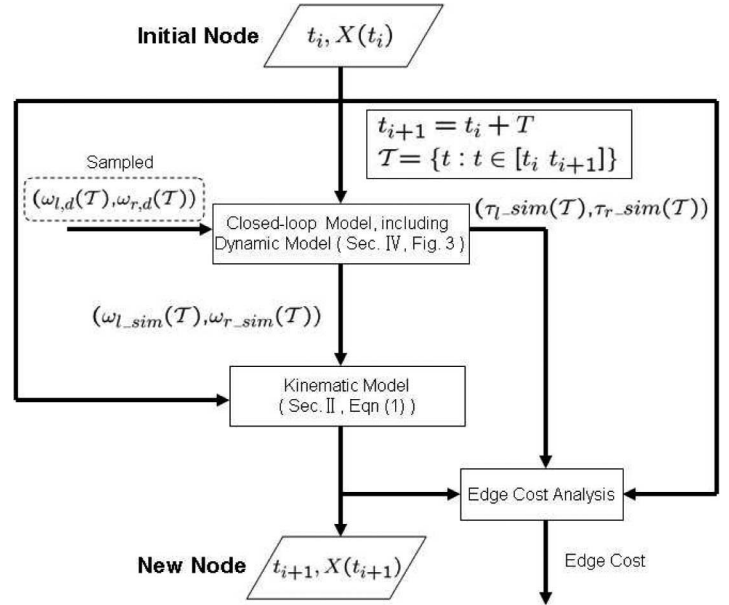Fig. 5. Speed versus torque curve for a dc motor.

Fig. 6. Calculation of the edge cost (distance traveled, time traveled, energy expended, etc.) for the SBMPC algorithm. (Notation: For a function $f(t)$ and a time interval $\mathcal{T}$, $f(\mathcal{T}) = \{f(t) : t \in \mathcal{T}\}$.)

and K_T, K_B, and R_a are the torque constant, voltage constant, and armature resistance, respectively. The shaded area in Fig. 5 is the safe working region, i.e., if the motor works outside of the shaded area continuously, the motor will overheat and will be in danger of burning out.

C. Motor Controller

The motor controller can be viewed as an electrical drive system for the motor. For speed control of the motor, the motor controller has two patterns: current control and voltage control. In this research, the current control pattern was used, as indicated in Fig. 3. The voltage signal from the PID controller is transferred into the current signal through the motor controller.

The Maxon 4-Q-dc motor controller has been utilized in this research and has a maximum output voltage $V_{m,\max}$, which is governed by

$$V_{m\_\max} = \mathrm{PWM}(V_{\mathrm{CC}} - U_{\mathrm{loss}}) - \frac{(\Delta n_m / \Delta \tau_m) K_T I_m}{K_n} \quad (27)$$

where PWM is the pulsewidth modulation, V_{CC} is the battery supply voltage, U_{loss} is the voltage loss in the motor controller, $\Delta n_m / \Delta \tau_m$ is the speed–torque gradient of the motor, and K_n is the speed constant. From Fig. 5, it is seen that $V_{m\_\max}$ controls the maximum speed of the motor.

D. Application of the Dynamic Models in Motion Planning

An important objective of this research is to develop dynamic models that are useful for motion planning. It is envisioned that these models will be used in conjunction with sampling-based model predictive control (SBMPC) [27], which is an input sampling algorithm that was designed to enable real-time motion planning using potentially complex dynamic models. In SBMPC, the nodes are states, and the edges are the inputs that cause the system to transition from one state (i.e., node) to another. An edge cost can be the distance traveled, the time traveled, the energy expended, etc., depending upon the global cost that is being optimized.

Fig. 6 shows how the closed-loop model and kinematic model are used to calculate the edge cost. Note that the kinematic model is needed to compute the simulated state $X(t_{i+1})$ and falls out-

side the feedback loops of the closed-loop model. In Fig. 6, the inputs at time t_i are the the current state $X(t_i)$ and the sampled, desired angular velocities of the left and right wheels $\omega_{l,d}(t)$ and $\omega_{r,d}(t)$ on the interval $\mathcal{T} = [t_i \ \ t_{i+1}]$, where $t_{i+1} = t_i + T$, and T is the planning sample period. Next, the closed-loop dynamic model of Fig. 3 is used to determine (on the interval $\mathcal{T}$) the simulated angular velocities of the left and right wheels $\omega_{l\_\mathrm{sim}}(t)$ and $\omega_{r\_\mathrm{sim}}(t)$ and the simulated torques of the left and right wheels $\tau_{l\_\mathrm{sim}}(t)$ and $\tau_{r\_\mathrm{sim}}(t)$. The kinematic model is then used to determine the next state $X(t_{i+1})$. The inputs and outputs of the closed-loop model and kinematic model blocks are used in the edge cost analysis block to compute the corresponding edge cost.

The kinematic model is used differently when evaluating a dynamic model. In particular, the inverse kinematic model is used as discussed later in Section V, regarding the experiments of Sections V-A and C, which are used to test the accuracy of the model for 2-D general motion.

V. EXPERIMENTAL VERIFICATION

This section describes parts of the experiments that have been conducted to verify the closed-loop control system, including the PID controller, motor controller, motor, vehicle dynamics, and terrain interaction. The model was simulated in SIMULINK to provide the theoretical results, which were compared with the experimental results.

The experimental platform is the modified Pioneer 3-AT shown in Fig. 7. The original, nontransparent, speed controller from the company was replaced by a PID controller and motor controller. PC104 boards replaced the original control system boards that came with the vehicle. Two current sensors were

Fig. 7. Modified Pioneer 3-AT entering a white-board ramp.

TABLE I
K, μ_{sa}, AND μ_{op} FOR DIFFERENT N ON VINYL LAB SURFACE

N	K	μ_{sa}	μ_{op}	N	K	μ_{sa}	μ_{op}
2	0.00060	0.4609	0.3186	7	0.00054	0.4437	0.3093
3	0.00051	0.4567	0.3193	8	0.00056	0.4321	0.3033
4	0.00064	0.4521	0.3113	11	0.00054	0.4323	0.3061
5	0.00061	0.4510	0.3109	16	0.00052	0.4208	0.2981
6	0.00059	0.4400	0.3083	31	0.00050	0.4151	0.2964

mounted on each side of the vehicle to provide real-time measurement of the motors' currents.

Let μ_{sa} denote the coefficient of friction for the wheels when the current and angular velocity of the motor have the same sign, such that the motor applies a propulsive force. Let μ_{op} denote the coefficient of friction for a wheel when the two have the opposite sign, resulting in the motor applying a braking force. The values of the parameters K, μ_{sa}, and μ_{op} are terrain-dependent and are difficult to determine by direct measurement. As a result, the values of K, μ_{sa}, and μ_{op} are computed by solving the nonlinear optimization problem

$$\min_{K, \mu_{\text{sa}}, \mu_{\text{op}}} \sum_{i=1}^{N} \left[\left(\Delta \tau_{l\_\text{Res}}^{(i)} \right)^2 + \left(\Delta \tau_{r\_\text{Res}}^{(i)} \right)^2 \right] \quad (28)$$

where i denotes the ith of N experiments, and $\Delta \tau_{l\_\text{Res}}^{(i)}$ and $\Delta \tau_{r\_\text{Res}}^{(i)}$ are the values of the difference between the steady-state simulation and experimental torques. The commanded turning radius R is defined as the turning radius resulting from applying the wheel speeds ω_l and ω_r to the kinematic model (2) assuming no slip. The set of experimental indexes i given by $\{1, 2, \ldots, 31\}$ map to the set of commanded turning radii R given by $\{0.2, 0.3, \ldots, 1, 2, \ldots, 10^1, 10^{1.2}, \ldots, 10^2, 10^{2.2}, \ldots, 10^{3.2}, 10^{3.6}, 10^4\}$. The optimal K, μ_{sa}, and μ_{op} for various values of $N \in \{2, 3, \ldots, 31\}$ were found using the MATLAB optimization toolbox function `lsqnonlin` and are given in Table I. For each N, the corresponding i were chosen to be evenly spaced. Although, as N increases, Table I shows that the values of these parameters (for the vinyl lab surface) appeared to converge, the variation from $N = 2$ to 31 is modest (16.7% for K, 9.9% for μ_{sa}, and 7.0% for μ_{op}). Hence, these results show that only

TABLE II
PARAMETERS FOR CLOSED-LOOP SYSTEM MODEL

Vehicle		
Mass (kg)	m	30.6
Moment of Inertia (kg·m²)	I	0.816
Width of vehicle (m)	B	0.40
Width of wheel (m)	b	0.05
Length of L (m)	L	0.31
Length of C (m)	C	0.24
Radius of tire (m)	r	0.1075
PID Controller		
Proportional gain	K_p	30.25
Integral gain	K_i	151.25
Derivative gain	K_d	0.0605
Motor		
Stall torque (Nm)	τ_s	0.2775
No-load speed (rad/s)	ω_n	487.16
Nominal voltage (V)	V_{nom}	12
Max Continuous Current (A)	I_{max}	5.5
Torque constant	K_T	0.023
Gear ratio	g_r	49.8
Moment of Inertia (kg·m²)	I_{motor}	0.000007
Viscous Damping (N·m/(rad/s))	D	0.000003
Motor Controller		
Pulse-width modulation	PWM	0.95
Vinyl Lab Surface		
Expansion factor	α	1.5
Shear deformation modulus (m)	K	0.00054
Coefficient of rolling resistance	$\mu_{roll,lab}$	0.0371
Coefficient of friction, of μ_{sa}	μ_{sa}	0.4437
Coefficient of friction, of μ_{op}	μ_{op}	0.3093
Asphalt Surface		
Coefficient of rolling resistance	$\mu_{roll,asphalt}$	0.051

a small number of experiments are needed to determine the coefficients of friction and shear moduli.

The other terrain-dependent parameter, i.e., coefficient of rolling resistance μ_{roll}, is computed by commanding a constant velocity to a vehicle going straight on a specific terrain. The rolling resistance is obtained from the average applied torque to the wheel. The coefficient of rolling resistance is then the rolling resistance divided by the weight of vehicle.

Since they are terrain-dependent, the coefficients of friction (μ_{sa} and μ_{op}), shear modulus (K), and coefficient of rolling resistance (μ_{roll}) must be determined for each surface via the aforementioned optimization procedure. Hence, the dynamic model changes with the terrain being traversed.

All of the key parameters for the model of the closed-loop system are listed in Table II. These parameters include the gains of the PID controller, which are the controller gains for the skid-steered vehicle of Fig. 7.

The experiments described in Sections V-A and C require the vehicle to traverse particular trajectories (circles in Section V-A and a lemniscate in Section V-C). These trajectories are characterized in terms of desired linear velocity $v_{y,d}$ and desired turning radius ρ_d. The inverse kinematic model was used, as shown in Fig. 8, at the sample instants to convert $v_{y,d}$ and ρ_d to the desired (i.e., commanded) velocities of the left and right wheels $\omega_{l,d}$ and $\omega_{r,d}$, which were then input to the closed-loop model of Fig. 3 to calculate the simulated velocities of the left and right wheels ω_{l_sim} and ω_{r_sim} along with the corresponding torques τ_{l_sim} and τ_{r_sim}.
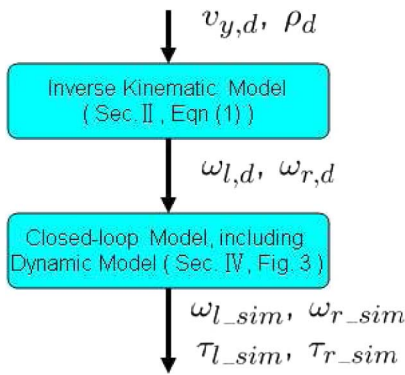
Fig. 8. Use of the inverse kinematic model to generate the desired left and right wheel velocities corresponding to the desired linear velocity $v_{y,d}$ and the desired turning radius ρ_d in Sections V-A and C.
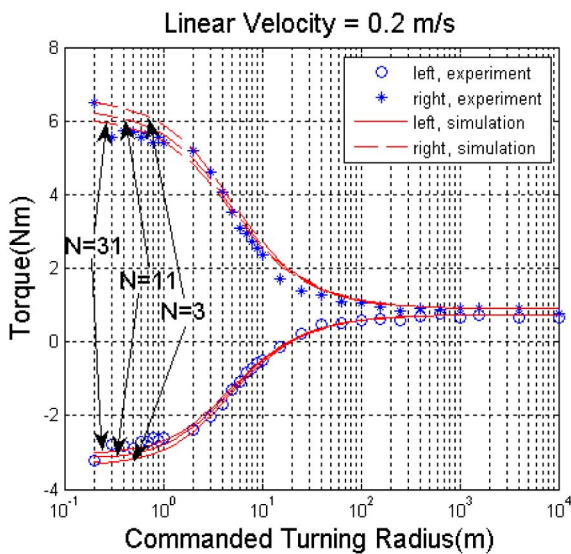

Fig. 9. Vehicle left and right wheel torque comparison during steady-state CCW rotation for different commanded turning radii on the lab vinyl surface.

Fig. 10. Closed-loop vehicle left and right wheels velocity comparison for 2-D circular movement on the lab vinyl surface.
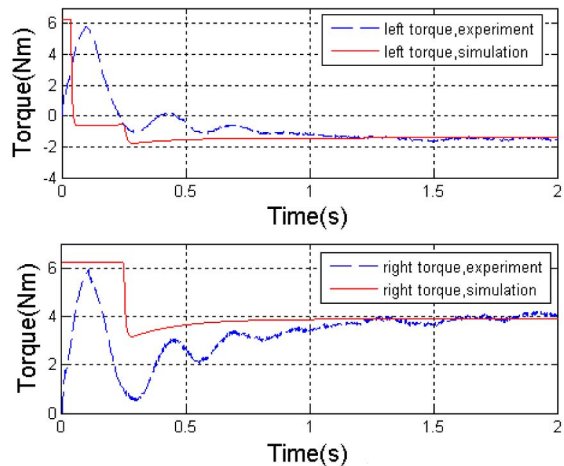
Fig. 11. Closed-loop vehicle left and right wheels torque comparison corresponding to Fig. 10.

A. 2-D Circular Movement

In this section, 2-D circular motion results are presented. When a skid-steered wheeled vehicle is in constant velocity circular motion, the left and right wheel torques are governed by (21) and (18), respectively. The theoretical and experimental torques for different commanded radii are shown in Fig. 9. If shear stress is not a function of shear displacement, but instead takes on a maximum value when there is a small relative movement between wheel and terrain, the left and right motor torques should be constant for different commanded turning radii, which is a phenomenon not seen in Fig. 9. Instead, this figure shows that the magnitudes of both the left and right torques reduce as the commanded turning radius increases. The same trend is found in [16] and [21].

The extreme case is that when the vehicle is in straight-line movement, the sliding friction is zero, and the motor torque only has to compensate for the rolling resistance torque. It should be mentioned that if the load transfer from the left wheel to the right wheel is not large, experimental results have shown that

the steady-state torques of the left and right wheels for different commanded turning radii are nearly the same for commanded linear velocities from 0.1 to 0.6 m/s, which is modeled accurately by (21) and (18).

Figs. 10–13 show the results when the vehicle is commanded to rotate at a constant velocity, beginning from a zero initial velocity. The commanded linear velocity and commanded radius to the vehicle are 0.2 m/s and 4 m on the lab vinyl surface. Note that there is some mismatch between the experimental and simulation velocities during the acceleration phase of the motion (<1 s). This is not surprising, since constant velocity was assumed in the development of the resistance term $C(q, \dot{q})$, and the experimental results of Fig. 10 correspond to a maximum acceleration greater than 3.39 m/s^2. Therefore, if the vehicle has large acceleration during rotation, the prediction becomes inaccurate for the acceleration period. It should be noted that our current models are fairly precise in taking into account the influence of acceleration through the mass matrix (i.e., by $M\ddot{q}$),
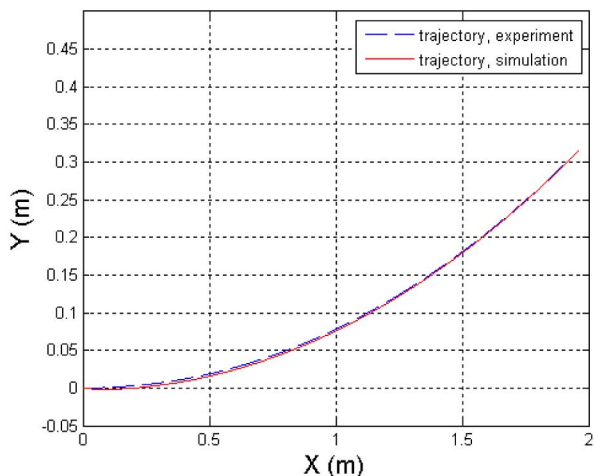
Fig. 12.   Closed-loop trajectory comparison corresponding to Fig. 10.
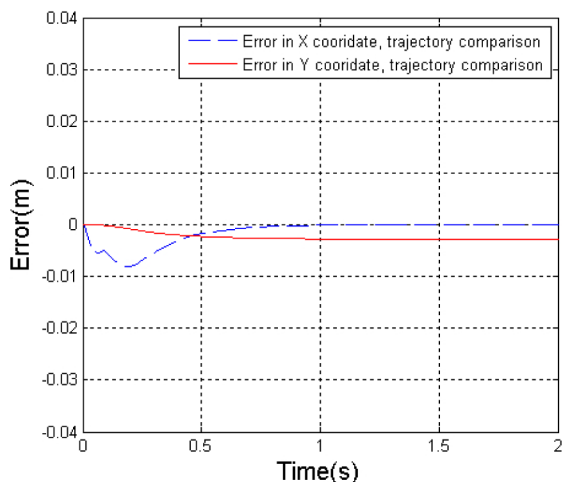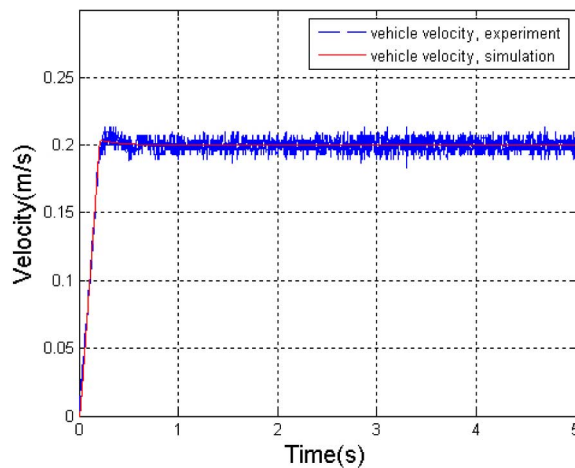

Fig. 14.   Closed-loop vehicle velocity comparison when the vehicle is commanded to 0.2 m/s for straight-line movement on the lab vinyl surface.
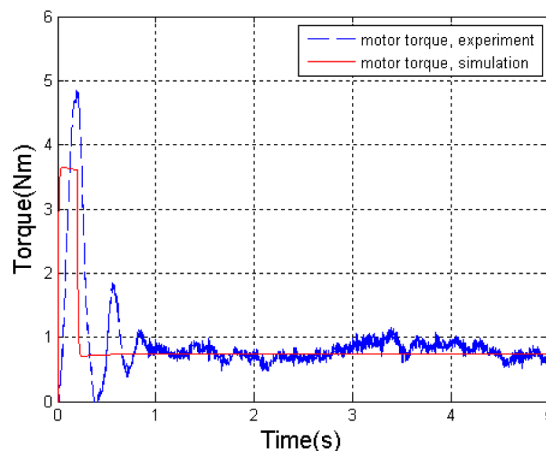

Fig. 13.   Closed-loop trajectory errors (experiment–simulation) in X and Y coordinates corresponding to the trajectories of Fig. 12.

Fig. 15.   Closed-loop motor torque comparison corresponding to Fig. 14.

which allows them to accurately describe acceleration when moving linearly and take into account some of the influence of acceleration when turning.

B. 2-D and 3-D Linear Movement

Figs. 14–16 show comparisons of both open-loop and closed-loop experimental and simulation results for linear 2-D motion. The vehicle is commanded at an acceleration of 1 m/s^2 to a velocity of 0.2 m/s for straight-line movement on the lab vinyl surface. Fig. 16 essentially uses the experimental torque of Fig. 15 as the system input. It is seen that the closed-loop system gives a much better prediction of the vehicle velocity than the open-loop system.

Fig. 17 shows the velocity comparison of closed-loop experimental and simulation results for linear 2-D motion when the vehicle is commanded to an unachievable velocity of 1.5 m/s. From Fig. 17, it can be seen that due to the saturation and power limitation of actuators, the vehicle can only reach the final velocity of around 0.93 m/s but not the desired 1.5 m/s. The kinematic model is incapable of this type of motion prediction,
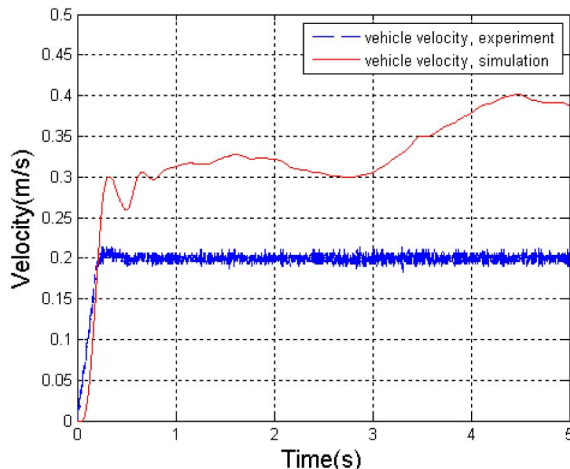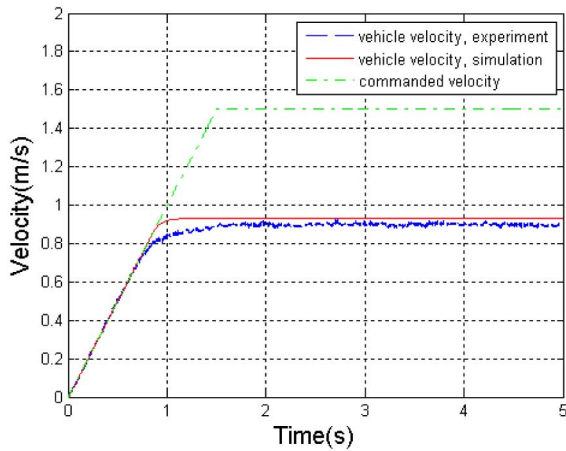

Fig. 16.   Open-loop vehicle velocity comparison when the vehicle is commanded with the voltage V that corresponds to the torque τ of Fig. 15. (In the open-loop model of Fig. 3, $\tau = K_\tau V$, where K_τ is a constant.)

Fig. 17. Closed-loop vehicle velocity comparison when the vehicle is commanded to 1.5 m/s for straight-line movement on the lab vinyl surface.
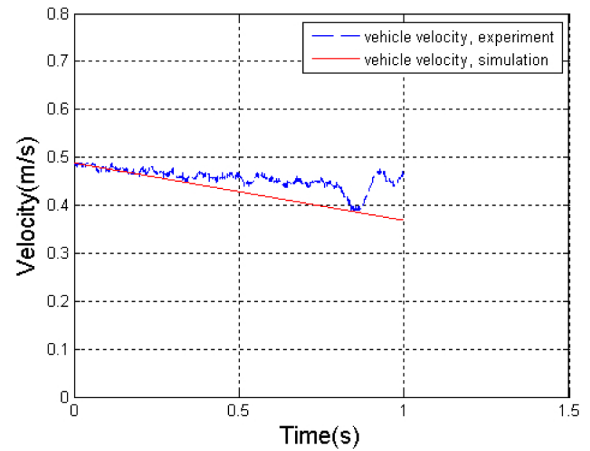

Fig. 19. Closed-loop vehicle velocity comparison when commanded linear velocity = 1.2 m/s with 0.49 m/s initial velocity for wood-board hill climbing with slope $\beta = 15.0°$.
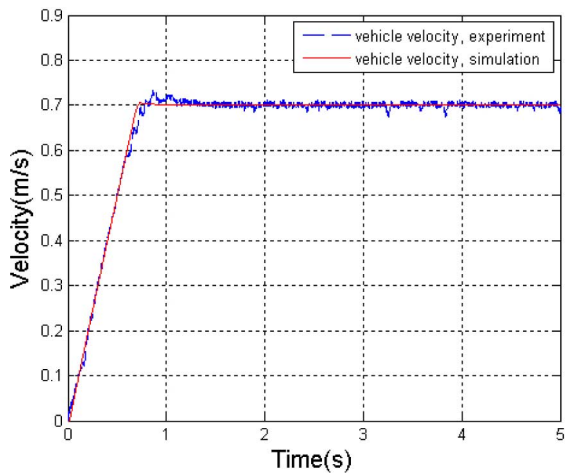

Fig. 18. Closed-loop vehicle velocity comparison when commanded linear velocity = 0.7 m/s for asphalt hill climbing with slope $\beta = 5.4°$.
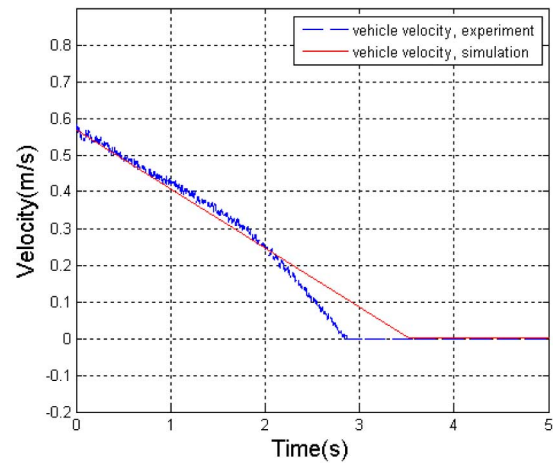

Fig. 20. Closed-loop vehicle velocity comparison when commanded linear velocity = 1.2 m/s with 0.57 m/s initial velocity for white-board hill climbing with slope $\beta = 13.5°$.

since it cannot take into account motor limitations. However, it is important to also recognize that even when the kinematic model yields accurate motion prediction, it does not yield the torque predictions that are key to energy-efficient motion planning.

Figs. 18–20 illustrate hill climbing for these three cases: 1) the ability to traverse a ramp at the commanded velocity; 2) the ability to traverse a ramp that is so steep that the vehicle decelerates while climbing, regardless of the commanded velocity; and 3) the inability to traverse a steep ramp because of inadequate initial velocity. These results clearly demonstrate the ability of the model to predict traversal times on undulating terrains and to predict the inability of the vehicle to traverse a steep hill.

C. 2-D Curvilinear Movement

In this section, the model is further tested for curvilinear motion. The vehicle was commanded to move in lemniscate trajectory. During the lemniscate movement, both the linear velocity and turning radius of the robot continuously change.

The chosen trajectory is described by

$$X(t) = \frac{9\cos(t/50)}{1 + \sin^2(t/50)} \tag{29}$$

$$Y(t) = \frac{27\sin(t/50)\cos(t/50)}{1 + \sin^2(t/50)} \tag{30}$$

where t is the time, and $(X(t), Y(t))$ is the position in global coordinates. The trajectory was chosen to test whether the dynamic model can give accurate predictions of velocities and torques when the vehicle is turning with linear and angular accelerations, since the resistance term in dynamic model is derived using a constant linear and angular velocity assumption. This trajectory was also chosen to ensure that the wheel velocities do not violate the motor power limitations, which leads to motor saturation during the motion. In addition, this trajectory tests a large range of vehicle velocities and turning radii.

Due to lab-surface limitations, the vehicle was required to traverse only part of the lemniscate. The three terrain parameters for the testing surface are $K = 0.0009$, $\mu_{\text{sa}} = 0.6488$, and
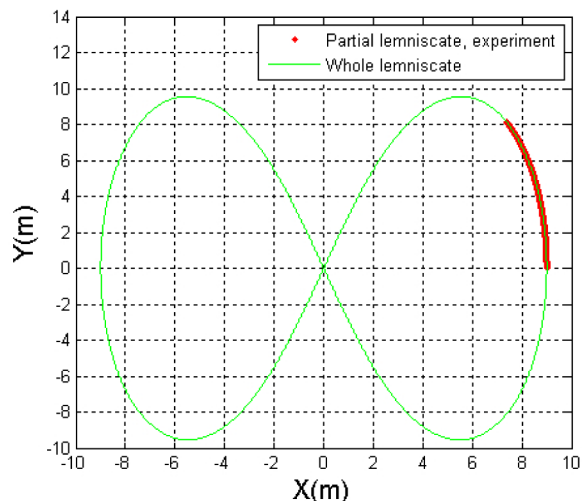
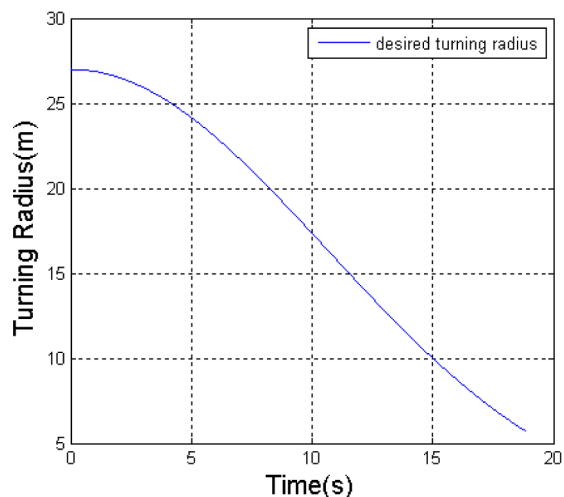Fig. 21. Partial and whole lemniscate trajectories.

Fig. 23. Desired turning radius corresponding to partial lemniscate in Fig. 21.
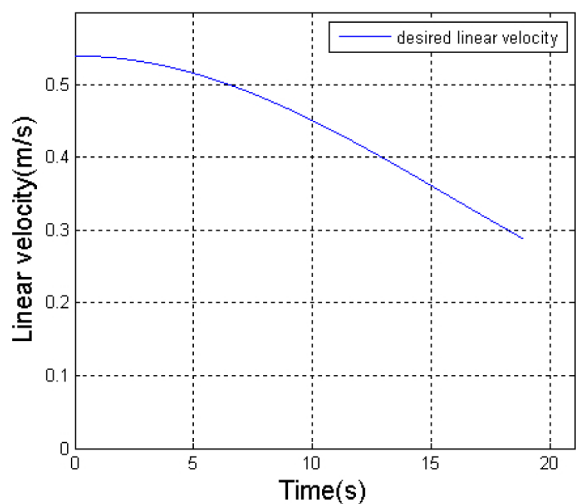

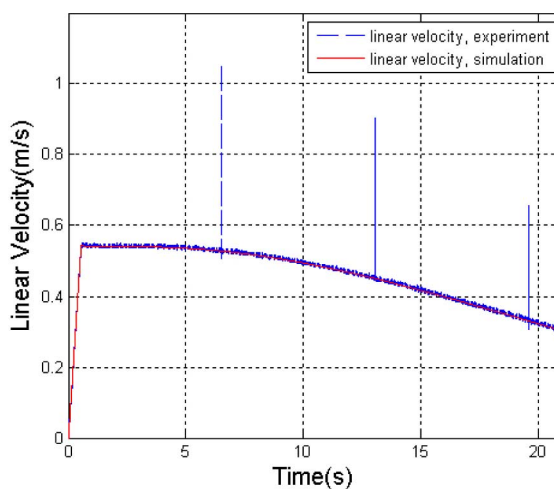Fig. 22. Desired linear velocity corresponding to partial lemniscate in Fig. 21.

Fig. 24. Closed-loop vehicle linear velocity comparison corresponding to lemniscate movement in Fig. 21.

$\mu_{\rm op} = 0.4601$. Fig. 21 shows the partial lemniscate trajectory used in the experiment and the complete lemniscate trajectory from (29) to (30). Figs. 22 and 23 show the desired linear velocity $v_{y,d}$ and desired turning radius ρ_d of the vehicle for the corresponding partial lemniscate trajectory in Fig. 21.

The vehicle was first commanded at an acceleration of 1 m/s^2 to achieve the initial velocity in Fig. 22 within 3 s. It was then commanded to follow the desired linear velocity and desired turning radius for 18 s, as shown in Figs. 22 and 23. Figs. 24 and 25 show linear velocity and angular velocity comparisons of the experimental and simulation results. Figs. 26–28 show the corresponding torque and trajectory comparisons. (Note that the experimental and simulation trajectories in Fig. 28 are indistinguishable.) Fig. 29 shows the trajectory error comparison in the X and Y coordinates corresponding to Fig. 28. From these results, it is seen that for the vehicle turning with continually changing acceleration (in the range [0 0.02] m/s^2), the model provides accurate predictions of velocities and reasonable predictions of torques.
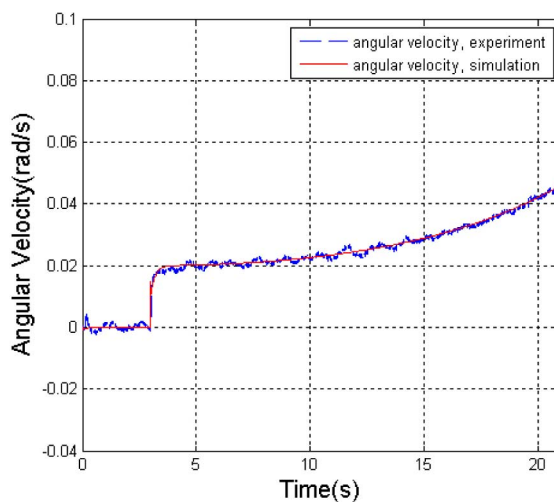

Fig. 25. Closed-loop vehicle angular velocity comparison corresponding to lemniscate movement in Fig. 21. (The experimental angular velocity was filtered with a low-pass filter $(1/(0.04s + 1))$ to reduce the noise.)
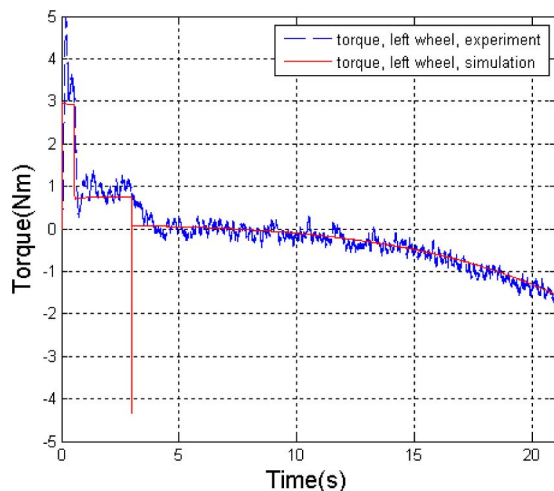
Fig. 26. Closed-loop left-wheel-torque comparison corresponding to lemniscate movement in Fig. 21.
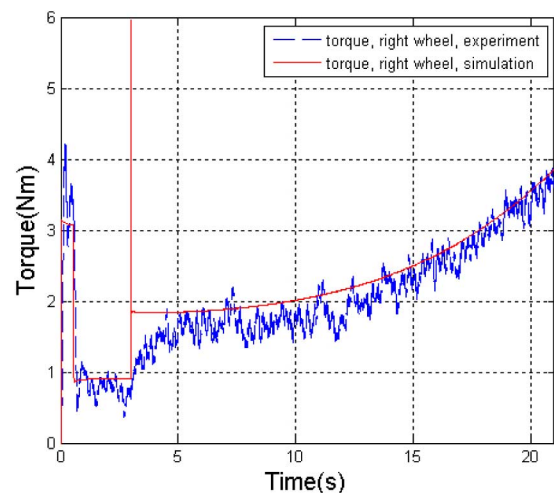

Fig. 27. Closed-loop right-wheel-torque comparison corresponding to lemniscate movement in Fig. 21.
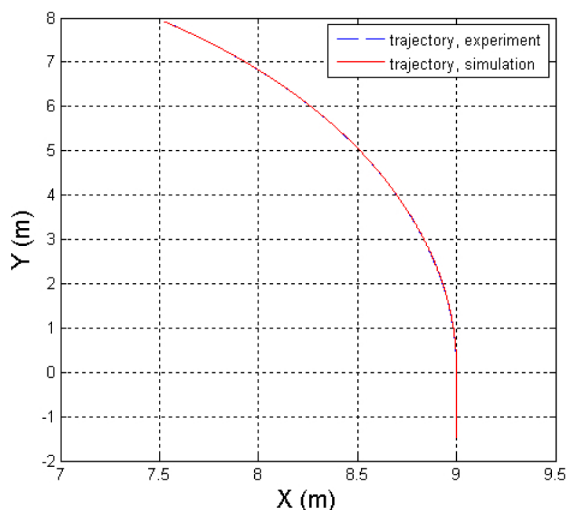

Fig. 28. Closed-loop trajectory comparison corresponding to lemniscate movement in Fig. 21.
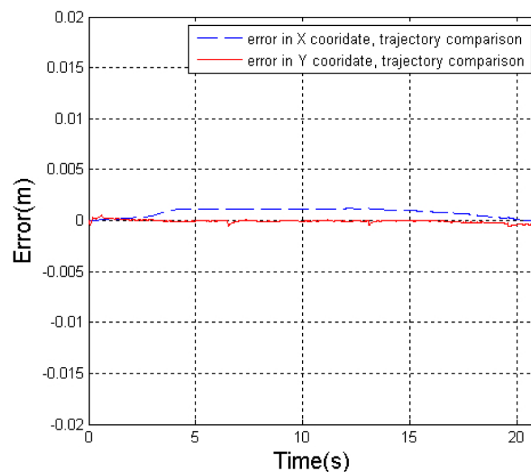

Fig. 29. Closed-loop trajectory errors (experiment–simulation) in X and Y coordinates corresponding to the trajectories of Fig. 28.

VI. CONCLUSION

This paper developed dynamic models for skid-steered wheeled vehicles for general 2-D motion and linear 3-D motion. An important contribution of this research is that unlike most previous research, these models were developed assuming a specific functional relationship between the shear stress and shear displacement and did not simply assume a constant (maximum) value for the shear stress when an arbitrarily small shear displacement occurs. The development of the resistance term $C(q, \dot{q})$ is similar to the results of [16] and [21] for constant velocity motion of skid-steered *tracked* vehicles. However, this research also considers the acceleration and gravitational terms in addition to taking into account the PID controller, the motor, and motor controller. Another contribution of this research is its focus on the closed-loop dynamics, which enables more accurate predictions of the vehicle velocity than that achievable with an open-loop model. The dynamic models are validated using extensive experimentation and seen to yield accurate predictions of velocity and reasonable predictions of torque.

One limitation of the research is that the resistance term was developed using a constant linear and angular velocity assumption, and hence, although the models tend to give good results for linear and curvilinear motions with small acceleration, they tend to lead to prediction inaccuracies when the vehicle has large acceleration during rotation, as shown in Fig. 10. Another limitation is that the resistance term only applies to hard terrains in which significant sinkage does not occur. In addition, no model was developed for general 3-D motion.

Future research will include online calibration of terrain-dependent parameters (coefficient of rolling resistance, coefficient of sliding friction, and shear deformation modulus) and develop a model for general 3-D motion. In addition, the models will be used for motion planning using SBMPC [27].

REFERENCES

[1] T. M. Howard and A. Kelly, "Optimal rough terrain trajectory generation for wheeled mobile robots," *Int. J. Robot. Res.*, vol. 26, no. 2, pp. 141–166, Feb. 2007.

[2] R. Siegwart and I. R. Nourbakhsh, *Introduction to Autonomous Mobile Robotics*. Cambridge, MA: MIT Press, 2005, ch. 2.

[3] B. Shamah, M. D. Wagner, S. Moorehead, J. Teza, D. Wettergreen, and W. R. L. Whittaker, "Steering and control of a passively articulated robot," in *SPIE, Sens. Fusion Decentralized Control Robot. Syst. IV*, vol. 4571, pp. 96–107, Oct. 2001.

[4] A. Mandow, J. L. Martłnez, J. Morales, J. Blanco, and A. J. Garcła-Cerezo, J. Gonzalez, "Experimental kinematics for wheeled skid-steer mobile robots," in *Proc. IEEE/RSJ Int. Conf. Intell. Robots Syst.*, San Diego, CA, 2007, pp. 1222–1227.

[5] Y. Zhang, D. Hong, J. H. Chung, and S. A. Velinsky, "Dynamic model-based robust tracking control of a differentially steered wheeled mobile robot," in *Proc. Amer. Control Conf.*, Philadelphia, PA, 1998, pp. 850–855.

[6] L. Caracciolo, A. D. Luca, and S. Iannitti, "Trajectory tracking control of a four-wheel differentially driven mobile robot," in *Proc. IEEE Int. Conf. Robot. Autom.*, Detroit, MI, 1999, pp. 2632–2638.

[7] J. T. Economou, R. E. Colyer, A. Tsourdos, and B. A. White, "Fuzzy logic approaches for wheeled skid-steer vehicle," in *Proc. Veh. Technol. Conf.*, Birmingham, AL, 2002, pp. 990–994.

[8] J. L. Martinez, A. Mandow, J. Morales, S. Pedraza, and A. Garcia-Cerezo, "Approximating kinematics for tracked mobile robots," *Int. J. Robot. Res.*, vol. 24, no. 10, pp. 867–878, Oct. 2005.

[9] P. Petrov, J. D. Lafontaine, P. Bigras, and M. Tetreault, "Lateral control of a skid-steering mining vehicle," in *Proc. IEEE/RSJ Int. Conf. Intell. Robots Syst.*, Takamatsu, Japan, 2000, pp. 1804–1809.

[10] J. Yi, J. Zhang, D. Song, and S. Jayasuriya, "IMU-based localization and slip estimation for skid-steered mobile robot," in *Proc. IEEE/RSJ Int. Conf. Intell. Robots Syst.*, San Diego, CA, 2007, pp. 2845–2849.

[11] K. Kozlowski and D. Pazderski, "Modeling and control of a 4-wheel skid-steering mobile robot," *Int. J. Appl. Math. Comput. Sci.*, vol. 14, no. 4, pp. 477–496, 2004.

[12] Z. Song, Y. H. Zweiri, and L. D. Seneviratne, "Nonlinear observer for slip estimation of skid-steering vehicles," in *Proc. IEEE Int. Conf. Robot. Autom.*, Orlando, FL, 2006, pp. 1499–1504.

[13] J. Yi, D. Song, J. Zhang, and Z. Goodwin, "Adaptive trajectory tracking control of skid-steered mobile robots," in *Proc. IEEE Int. Conf. Robot. Autom.*, Roma, Italy, 2007, pp. 2605–2610.

[14] O. Chuy, E. G. Collins, W. Yu, and C. Ordonez, "Power modeling of a skid steered wheeled robotic ground vehicle," in *Proc. IEEE Int. Conf. Robot. Autom.*, Kobe, Japan, 2009, pp. 4118–4123.

[15] S. Golconda, "Steering control for a skid-steered autonomous ground vehicle at varying speed," Master's thesis, Univ. Louisiana at Lafayette, Lafayette, LA, 2005.

[16] J. Y. Wong, *Theory of Ground Vehicles*, 3rd ed. New York: Wiley, 2001.

[17] D. Endo, Y. Okada, K. Nagatani, and K. Yoshida, "Path following control for tracked vehicles-based slip-compensation odometry," in *Proc. IEEE/RSJ Int. Conf. Intell. Robots Syst.*, San Diego, CA, 2007, pp. 2871–2876.

[18] S. A. A. Moosavian and A. Kalantari, "Experimental slip estimation for exact kinematics modeling and control of a tracked Mobile Robot," in *Proc. IEEE/RSJ Int. Conf. Intell. Robots Syst.*, Nice, France, 2008, pp. 95–100.

[19] K. Nagatani, D. Endo, and K. Yoshida, "Improvement of the odometry accuracy of a crawler vehicle with consideration of slippage," in *Proc. IEEE Int. Conf. Robot. Autom.*, Rome, Italy, 2007, pp. 2752–2757.

[20] X. Song, Z. Song, L. Senevirante, and K. Althoefer, "Optical flow-based slip and velocity estimation technique for unmanned skid-steered vehicles," in *Proc. IEEE/RSJ Int. Conf. Intell. Robots Syst.*, Nice, France, 2008, pp. 101–106.

[21] J. Y. Wong and C. F Chiang, "A general theory for skid steering of tracked vehicles on firm ground," *Proc. Inst. Mech. Eng., Part D, J. Automobile Eng.*, vol. 215, pp. 343–355, 2001.

[22] H. Wang, J. Zhang, J. Yi, D. Song, S. Jayasuriya, and J. Liu, "Modeling and motion stability analysis of skid-steered mobile robots," in *Proc. IEEE Int. Conf. Robot. Autom.*, Kobe, Japan, 2009, pp. 4112–4117.

[23] W. Yu, O. Chuy, E. G. Collins, and P. Hollis, "Dynamic modeling of a skid-steered wheeled vehicle with experimental verification," in *Proc. IEEE/RSJ Int. Conf. Intell. Robots Syst.*, St. Louis, MO, 2009, pp. 4211–4219.

[24] J. Morales, J. L. Martinez, A. Mandow, A. Garcia-Cerezo, J. Gomez-Gabriel, and S. Pedraza, "Power analysis for a skid-steered tracked mobile robot," in *Proc. Int. Conf. Mechatron.*, Budapest, Hungary, 2006, pp. 420–425.

[25] J. J. Craig, *Introduction to Robotics: Mechanics and Control*, 3rd ed. Englewood Cliffs, NJ: Prentice-Hall, 2004, ch. 9.

[26] G. Rizzoni, *Principles and Applications of Electrical Engineering*, 3rd ed. New York: McGraw-Hill, 2000, ch. 17.

[27] D. D. Dunlap, E. G. Collins, and C. V. Caldwell, "Sampling-based model predictive control with application to autonomous vehicle guidance," presented at the Florida Conf. Recent Adv. Robot., Melbourne, FL, 2008.
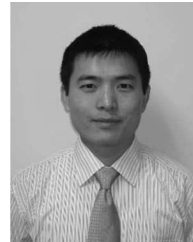
Wei Yu (S'09) received the B.S. and M.S. degrees in mechanical engineering from Hefei University of Technology, Hefei, China, in 2003 and 2006, respectively. He is currently working toward the Ph.D degree with the Department of Mechanical Engineering, Florida State University, Tallahassee.

His current research interests include dynamic system modeling and intelligent control, autonomous mobile robotics, kinodynamic path planning, and mechatronics.

Oscar Ylaya Chuy, Jr. (M'06) received the B.S.E.C.E. and B.S.E.E. degrees from Mindanao State University-Iligan Institute of Technology (MSU-IIT), Iligan City, the Philippines, the M.S.E.E. degree from the University of the Philippines, Quezon City, the Philippines, and the Ph.D. degree in bioengineering and robotics from Tohoku University, Sendai, Japan, in 2006.

From 1995 to 1997 and from 2000 to 2002, he was an Instructor at MSU-IIT. From 2006 to 2007, he was a Research Associate with the Department of Bioengineering and Robotics, Tohoku University. He is currently a Postdoctoral Research Associate with the Department of Mechanical Engineering, Florida A&M University-Florida State University, College of Engineering, Tallahassee. His research interests include human robot system, mobile robot control, and the application of robotics to healthcare.

Emmanuel G. Collins, Jr. (S'83–M'86–SM'99) received the Ph.D. degree in aeronautics and astronautics from Purdue University, West Lafayette, IN, in 1987.

He was with the Controls Technology Group, Harris Corporation, Melbourne, FL, for seven years. He joined the Department of Mechanical Engineering, Florida A&M University-Florida State University, College of Engineering, Tallahassee, where he is currently a John H. Seely Professor and the Director of the Center for Intelligent Systems, Control and Robotics. His research interests include navigation and control of autonomous vehicles (ground, water, and air) in extreme environments and situations, multi-robot and human–robot cooperation, and the control of aeropropulsion systems. He is the author or coauthor of more than 200 technical publications in control and robotics.

Dr. Collins was also an Associate Editor of the IEEE Transactions on Control System Technology from 1992 to 2001. In 1991, he received the Honorary Superior Accomplishment Award from the National Aeronautics and Space Administration Langley Research Center demonstrating active control of flexible spacecraft.

Patrick Hollis received the Ph.D. degree in mechanical engineering from Cornell University, Ithaca, NY, in 1986.

He is currently the Undergraduate Program Coordinator with the Department of Mechanical Engineering, Florida A&M University-Florida State University, College of Engineering, Tallahassee. His current research interests include dynamic systems and applications modeling and simulation.

Dr. Hollis is a member of the American Society of Mechanical Engineers and the Society of Automotive Engineers.